

Using tensor light shifts to measure and cancel a cell's quadrupolar frequency shift

S. K. Peck, N. Lane, D. G. Ang,^{*} and L. R. Hunter*Department of Physics, Amherst College, Amherst, Massachusetts 01002, USA*

(Received 22 December 2015; revised manuscript received 23 January 2016; published 25 February 2016)

We have developed a technique that uses the tensor light shift to measure and cancel the frequency shift produced by the quadrupolar anisotropy of a vapor cell. We demonstrate the technique on the $6S_{1/2}$, $F = 4$ level of Cs using the D_1 transition. The method extends our ability to study quadrupolar wall interactions beyond diamagnetic atoms. We have deduced the twist angle per wall adhesion for cesium on an alkene coating to be $\theta_{\text{Cs-alkene}} = 1.4$ mrad. This value is about 37 times larger than the twist angle observed in ^{131}Xe , suggesting that it is not produced by the interaction of the nuclear quadrupole moment with a collisional electric-field gradient. Alternative mechanisms that may be responsible for the observed quadrupolar frequency shifts are discussed. By canceling the cell-induced quadrupole shift we have extended our cells' effective spin-relaxation times by as much as a factor of 2. This cancellation improves magnetometer sensitivity in highly anisotropic cells and could reduce systematic uncertainties in some precision measurements.

DOI: [10.1103/PhysRevA.93.023426](https://doi.org/10.1103/PhysRevA.93.023426)

I. INTRODUCTION

High-precision magnetometers based on optically pumped atomic vapors have been used in diverse fields, including searches for violations of fundamental symmetries caused by non-standard model interactions [1–3]. In weak magnetic fields, the splittings between adjacent magnetic sublevels of an otherwise unperturbed atomic state are equal. This results in a uniform precession of the atomic polarization, which is the basis of most precision magnetometers. The sensitivities of these experiments and devices are often limited by the finite lifetime of the atomic polarization. Usefully long lifetimes can be achieved by introducing a buffer gas to limit the rate of collisions with the cell walls, or by coating the walls with materials such as paraffin or silane to inhibit the relaxation of the polarization during the wall collision. In vapor cells without buffer gas, the polarization relaxation time depends on the size and shape of the cell. If the shape of an atomic vapor cell has a significant quadrupolar anisotropy and the total angular momentum, F , is greater than $1/2$, collisions with the cell walls can introduce a quadrupolar splitting between magnetic sublevels resulting in multiple frequencies of precession and a dephasing of the atomic coherence. This dephasing reduces the effective spin-relaxation time of the state. Spin relaxation and dephasing associated with quadrupolar wall interactions have been extensively studied in diamagnetic atoms [4–16]. The longest spin-relaxation times observed for alkali atoms have been achieved in spherical cells, suggesting that quadrupolar dephasing effects may be important for paramagnetic atoms [17], but the mechanisms responsible for shorter spin-relaxation times in other cell geometries have not previously been studied. The much longer polarization-relaxation times observed in diamagnetic atoms suggest that the relevant relaxation mechanisms differ substantially.

Atomic light shifts have played an important role in a number of recent experiments involving vapor cells. The effects of light shifts have been well understood since the

pioneering work of Happer, Mathur, and Tang [18,19]. Vector light shifts, usually associated with circularly polarized light, lead to linear shifts in the magnetic sublevels that can be characterized by an “equivalent magnetic field” along the light beam. These have been used to measure the adsorption time of spin-polarized rubidium on coated glass surfaces [20]. Tensor light shifts are usually associated with linearly polarized light and lead to quadratic shifts of the magnetic sublevels. Tensor light shifts were used to calibrate measurements of cell-induced quadrupolar splittings in ^{201}Hg [21]. Measurements in rubidium [22] and cesium [23] used the tensor light shift in the far-detuned limit to cancel the nonlinear Zeeman effect. In this work we use the tensor light shift to measure and cancel the quadrupolar splitting caused by the atom-wall interaction in Cs vapor cells which have significant quadrupolar anisotropy, thereby demonstrating the measurement of a cell-shape-induced quadrupole splitting (CIQS) in a paramagnetic atom. Measurement of the CIQS provides a sensitive probe to investigate the interaction of paramagnetic atoms with surfaces. Our technique could facilitate measurements of the electric fields and/or electric-field gradients experienced by an atom during a wall collision. Such measurements could be helpful in understanding frequency shifts in cell-based secondary frequency standards [24]. The ability to cancel the CIQS in a vapor cell would allow experiments to use vapor cells with shapes having large quadrupolar anisotropy without suffering rapid quadrupolar dephasing. This cancellation technique could find applications in situations where nonspherical cells are required in order to obtain nondistorting optics, homogeneous electric fields, or the close proximity of several cells [25–28].

II. EXPERIMENTAL SETUP AND DATA COLLECTION

Many different optical-pumping schemes have been applied in atomic precession experiments [1]. The pump-then-probe (PTP) scheme is particularly well suited to the present investigation. In the most common PTP geometry [Fig. 1(a)] one places the vapor cell in an applied magnetic field \mathbf{B} (along z) and optically pumps the vapor with a resonant circularly polarized laser beam with wave vector \mathbf{k} (along y). Intensity

^{*}Current address: Department of Physics, Harvard University, Cambridge, Massachusetts 02138, USA.

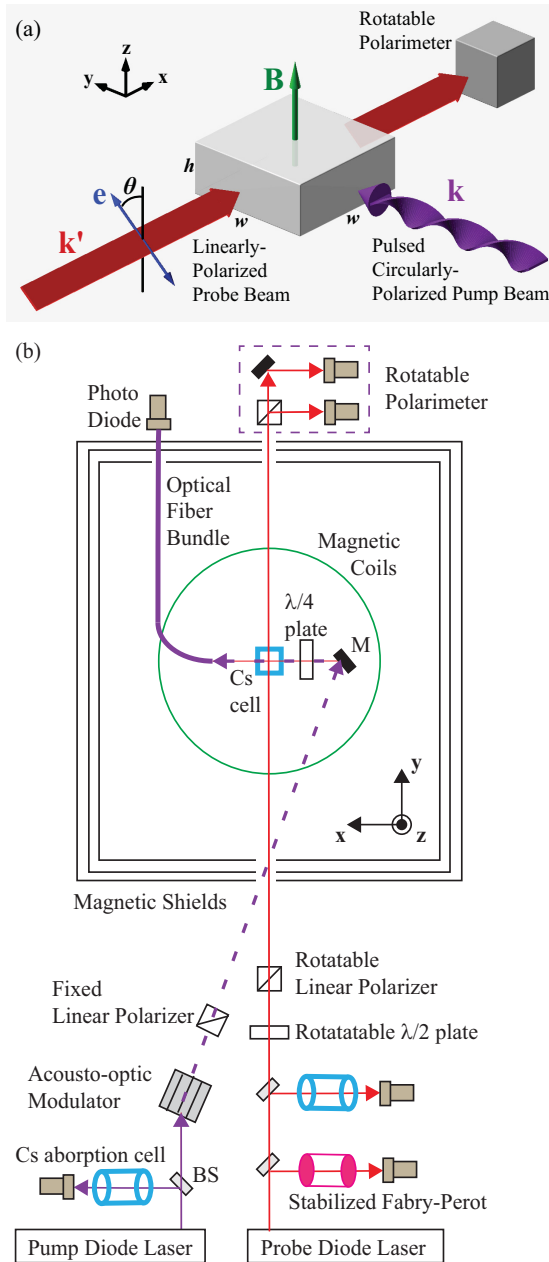


FIG. 1. (a) The experimental geometry. The pump and probe propagation directions are \mathbf{k} and \mathbf{k}' . θ is the angle between the applied magnetic field, \mathbf{B} , and the axis of the probe's linear polarization, \mathbf{e} . A cuboid cell with height h and width and depth both equal to w is shown. Here the cell's symmetry axis is along \mathbf{B} . (b) A schematic of the apparatus (not to scale). The dark (M) and shaded (BS) small rectangles are mirrors and beam splitters.

modulating the pump laser at the Larmor frequency creates a highly polarized sample precessing in the x - y plane. After the pump cycle, the pump laser beam is blocked and the sample is probed with a weak, far-detuned, linearly polarized beam with wave vector \mathbf{k}' (also perpendicular to \mathbf{B}) and polarization vector \mathbf{e} . The precessing atomic polarization modulates the vapor's index of refraction at the Larmor frequency, generating an oscillating optical-rotation signal that is measured with a polarimeter. With the probe beam far detuned from an isolated

absorption line the optical rotation decreases as the inverse of the detuning while the absorption decreases as the inverse of the detuning squared. Far detuning allows the probing of the atomic coherence in optically thick vapors without reducing the precession coherence time by absorption from the probe beam. The longer the atomic precession persists, the more precisely the precession frequency can be measured.

We have constructed a cesium magnetometer using the PTP scheme on the Cs D_1 line, modeled on the Rb magnetometer described by Kimball *et al.* [29]. A schematic of the apparatus is shown in Fig. 1(b). Our probe propagation direction \mathbf{k}' is along x , the symmetry axis of our cylindrical magnetic shields. The Cs vapor cell is mounted in the center of this assembly. Magnetic coils within the shields produce the homogeneous magnetic field, \mathbf{B} , that has a magnitude of about 6.0 mG [27]. The angle between the probe's linear polarization axis, \mathbf{e} , and the magnetic field, \mathbf{B} , is θ . The probe beam traverses the cell perpendicular to the vapor cell's axis of symmetry. This leads to a volume-averaged intensity within the vapor cell, $\bar{I} = P/A$, where A is area, P is the average power of the probe laser within the cell, and the effective area is $A = \pi dh/4$ for a cylinder with diameter d and height h , while $A = hw$ for symmetric cuboids with width and depth both equal to w and height h [22]. No buffer gas has been added to the cells but the inner walls of the cells have been coated with either an alkene or polyethylene coating to reduce spin relaxation due to wall collisions [17].

The 894-nm D_1 light for the pump and probe beams is generated using two home-built cavity-stabilized diode lasers. The pump laser is locked to the center of the $6S_{1/2}$, $F = 3$ to $6P_{1/2}$, $F' = 4$ transition using a Cs absorption cell. The pump beam is intensity modulated (20% duty cycle) at the Larmor frequency using an acousto-optic modulator and, then it passes through a linearly polarizing prism and quarter-wave plate to generate circular polarization before entering the vapor cell. The transmitted pump light is collected on an optical fiber bundle that transports the light out of the magnetic shields. The fiber-bundle output is monitored with a photodiode.

For a given data point, the probe beam frequency is set in the region of the $6S_{1/2}$, $F = 4$ to $6P_{1/2}$, $F' = 3$ and $F' = 4$ transitions. We measure the probe frequency, ν , relative to the frequency midway between these two hyperfine transitions. The probe beam frequency is monitored using a stabilized Fabry-Perot cavity and a Cs absorption cell. The intensity of the probe beam can be varied by rotating a half-wave plate before the rotatable linear polarizer that defines \mathbf{e} . With our cuboid cells, the light from the probe beam traverses the cell in the center of the shields and then travels about 0.6 m to a polarimeter outside of the magnetic shields. The input of the polarimeter consists of a polarizing beam splitter that separates the two orthogonal linear polarizations of the probe beam. The polarimeter is on a rotatable mount so that the polarizing beam splitter can be oriented with its polarization axis at 45° with respect to the probe's polarization axis, \mathbf{e} . This orientation results in nearly equal intensities in the beam splitter's transmitted and reflected beams. These orthogonally polarized beams are incident on two separate photodiodes and the difference between the photodiode currents is converted to a voltage and amplified. The resulting voltage, $V(t)$, is proportional to the optical rotation of the probe beam. For

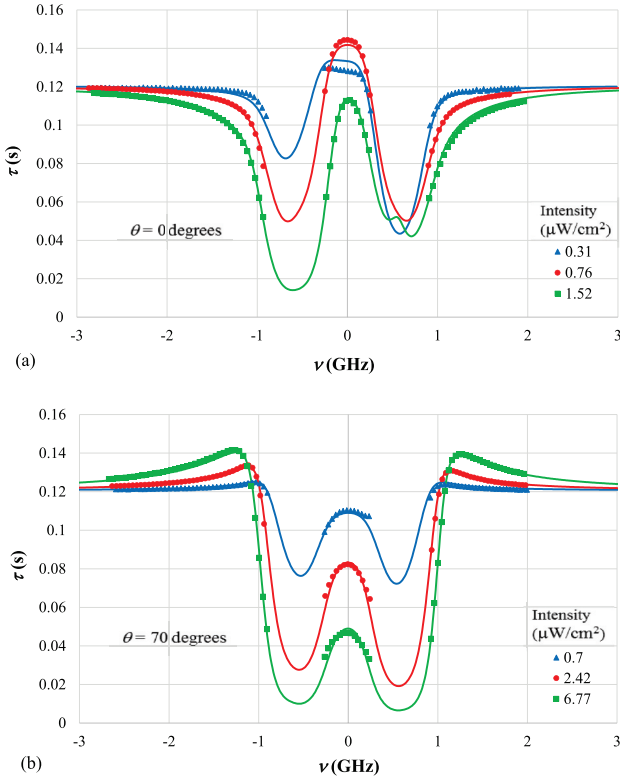


FIG. 2. The points are the measured values of τ at various probe frequencies. The cell's quadrupole axis is aligned with \mathbf{B} ($\alpha = 0$). The data in (a) and (b) are taken, respectively, with $\theta = 0^\circ$ and $\theta = 70^\circ$. The solid lines are the fits from the model described in Appendix.

cylindrical and spherical cells, the optical distortions caused by their curved surfaces prevent the probe beam from propagating outside the magnetic shields, so we place the polarizing beam splitter just after the cell and collect the light on two multimode optical fiber bundles [not shown in Fig. 1(b)] for transportation to the photodiodes.

To collect data on the polarization decay time, we extinguish the pump beam after synchronously pumping the atoms for 0.4 s. For the next 0.3 s the polarimeter output voltage is collected, digitized, and fit (LABVIEW) to a decaying, oscillating exponential with an offset term:

$$V(t) = V_0 + V \cos(2\pi ft + \delta)e^{-t/\tau}. \quad (1)$$

Here V is the modulation amplitude, f and δ are the frequency and phase of the precession, and τ is the effective spin-relaxation time. We refer to the spin-relaxation time as “effective” because the decay associated with the quadrupolar dephasing is not genuinely exponential but is in fact a superposition of eight different beat frequencies. However, we find that our signals are adequately approximated by simply using an effective spin-relaxation time in Eq. (1) (see Appendix A).

In each data scan we make many measurements of $V(t)$ at different probe frequencies. Measured values for τ as a function of ν are shown as points in Fig. 2. When the probe is far detuned, τ is largely independent of the detuning. As expected, τ decreases when the probe frequency is near the hyperfine transition resonances that are centered at $\nu =$

± 0.584 GHz. It would seem surprising that for some probe intensities and frequencies [e.g., $\bar{I} = 0.76 \mu\text{W}/\text{cm}^2$, $\nu = 0$, and $\theta = 0$ in Fig. 2(a) or $\bar{I} = 6.77 \mu\text{W}/\text{cm}^2$, $|\nu| = 1.3$ GHz, and $\theta = 70^\circ$ in Fig. 2(b)], τ can be greater than in the far-detuned limit. We have confirmed that when the atoms are allowed to precess in the dark (without the probe beam on), the measured τ agrees with the value obtained when the probe laser is far detuned. For certain combinations of probe frequency, polarization, and intensity the presence of the probe light actually increases τ . We have studied this effect and conclude that this increase of τ occurs due to cancellation of the CIQS with the quadratic splitting produced by the probe's tensor light shift. Below we outline the measurements and theory leading to this conclusion.

III. THEORETICAL BACKGROUND

If the Zeeman frequency shift induced by the applied magnetic field is small compared to the hyperfine splitting of the ground state, it is well approximated by the expression $\Delta\nu_{\text{Zeeman}} \approx \pm \frac{2}{2I+1} \mu_B m_F B$ where $I = 7/2$ is the nuclear spin of Cs, μ_B is the Bohr magneton, and m_F is the magnetic sublevel of the total angular momentum $F = I \pm 1/2$. This produces a spin-precession frequency of about 350 kHz/G in the ground state of Cs. If the Zeeman shift is large compared to the tensor light shift, the tensor light effect can be treated as a small perturbation, shifting the frequencies of the various magnetic sublevels m_F by

$$\Delta\nu_{\text{Stark}} = A(\nu)[3m_F^2 - F(F+1)][3\cos^2(\theta) - 1]\bar{I}, \quad (2)$$

where \bar{I} is the cell-averaged intensity experienced by the atoms [23,30]. In our experiment the relative shifts associated with the upper-state hyperfine splitting, $\Delta\nu_{\text{Zeeman}}$, $\Delta\nu_{\text{Stark}}$ and the nonlinear Zeeman effect [23] are, respectively, of order 1.2 GHz, 2.1 kHz, ~ 1 Hz, and 1 mHz, justifying the approximations used. We calculate $A(\nu)$ for $F = 4$ (Fig. 3) following the formalism of Mathur, Happer, and Tang [18,19] and using the measured values of the Cs $6P_{1/2}$ lifetime [31] and hyperfine splitting [32]. We have confirmed that our calculated value of A for $F = 3$ is in agreement with that of Chalupczak

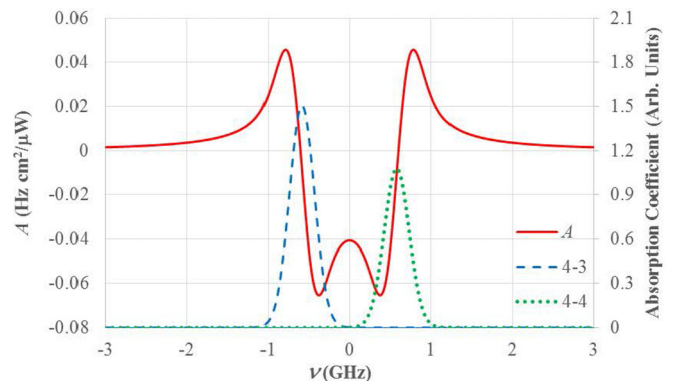


FIG. 3. The calculated tensor light shift coefficient $A(\nu)$ is a solid (red) line. The theoretical Voigt absorption profiles at 297 K for the $F = 4$ to $F' = 3$ and $F = 4$ to $F' = 4$ hyperfine transitions are denoted, respectively, by $V_3(\nu)$, a dashed (blue) line, and $V_4(\nu)$, a dotted (green) line.

et al., which was calculated at a single frequency in the large detuning limit [23].

The results of Wu *et al.* [33] can provide a phenomenological description of the quadrupolar energy shift associated with collisions with the cell's walls. We assume that our cells are either cylinders, or cuboids with two degenerate dimensions, such that the alignment of their quadrupolar anisotropy can be defined by a single symmetry axis (\mathbf{z}'). If we further assume that the quadrupole splitting created by the cell is small compared to the Zeeman splitting, we can express its frequency shift in a notation similar to Eq. (2) as

$$\Delta\nu_C = C[3m_F^2 - F(F+1)][3\cos^2(\alpha) - 1], \quad (3)$$

where α is the angle between \mathbf{z}' and \mathbf{B} and the constant C expresses the strength and sign of the cell-induced quadratic splitting. We note that the similar quadratic dependence on m_F of Eqs. (2) and (3) suggests that for appropriate values of the frequency and intensity it should be possible to make the effects cancel and eliminate the associated dephasing of the atomic polarization, thereby increasing its coherence time.

IV. UNDERSTANDING THE OBSERVED FREQUENCY AND INTENSITY DEPENDENCE OF τ

There are several interesting qualitative features of our data that suggest that the unusual behavior of τ is a consequence of a cancellation between the CIQS and the tensor light shifts created by the probe beam. First, when θ is near the “magic angle,” $\theta_M = \cos^{-1}(\sqrt{1/3}) \approx 54.7^\circ$, all tensor light effects should disappear. Without the tensor light shift there is no way to cancel the CIQS. Indeed, at θ_M we observe no enhanced values of τ at any probe-laser frequency. Next, we note that the tensor light shift line shape in Fig. 3 has the opposite sign at $\nu = 0$ and in the “wings,” the regions above and below the pair of hyperfine transitions where $|\nu| > 585$ MHz. As illustrated in Fig. 2(a), when $\theta < \theta_M$ and the cell's principle quadrupole axis \mathbf{z}' is aligned with \mathbf{B} ($\alpha = 0$), we find enhanced values of τ at $\nu = 0$ and suppressed values of τ in the wings. This suggests that the light shift has the opposite sign to the CIQS at the line center and the same sign in the wings, as is expected. When the intensity is such that the light shift at $\nu = 0$ exactly cancels the cell's quadratic shift, there is no dephasing and we

achieve a maximum value of the effective spin-relaxation time, τ_{\max} . When $\theta = 70^\circ$ (i.e., $\theta > \theta_M$) we expect the sign of the tensor light shift to reverse [Eq. (2)]. Now cancellation of the quadratic shift is only possible in the wings and the quadratic dephasing will increase at $\nu = 0$, so we expect suppression of τ at $\nu = 0$ and enhancement in the wings, as we see in Fig. 2(b).

To quantitatively predict the dependence of τ on the frequency, intensity, and polarization angle θ , we have developed a simple model where there are three decay rates that contribute to the effective decay of the spin. We assume there is (1) a scalar rate $R_{\min} = 1/\tau_{\max}$ that is independent of frequency and intensity, (2) a depolarization rate R_a that is proportional to the rate of absorption on the atomic resonance lines, and (3) an effective decay rate R_Q that depends on the size of the total quadratic splitting induced in the atoms by the sum of the light shift and a frequency-independent CIQS. Our model values of τ are determined using the expression $\tau = 1/(R_{\min} + R_a + R_Q)$. The details of the model are described in Appendix A and the resulting fits are shown as the solid lines in Figs. 2(a) and 2(b). For reasonable values of the experimental parameters the model successfully describes the frequency, intensity, and θ dependence of τ , providing confidence in our identification of the critical elements that contribute to the polarization decay.

V. MEASUREMENTS IN DIFFERENT CELLS AND CONFIGURATIONS

We have developed a quick and simple method for determining the CIQS that does not require a full fit of the entire spectrum. The data in Fig. 2(a) suggest that at $\nu = 0$ there is a specific compensating intensity, \bar{I}_c , that yields a maximum value of the effective relaxation time, τ_{\max} . While other frequencies could be used for this measurement, the point at $\nu = 0$ is particularly convenient as the slope $\frac{dA}{d\nu} = 0$ and there is little absorption to confuse the interpretation. We expect to minimize the quadrupolar dephasing and achieve τ_{\max} when the sum of the quadrupolar shifts cancel, $\Delta\nu_C + \Delta\nu_{\text{Stark}} = 0$. Applying this compensation condition at $\nu = 0$ yields an expression for the amplitude of the CIQS, $C = -A(0)(3\cos^2\theta - 1)\bar{I}_c/(3\cos^2\alpha - 1)$. We deduce \bar{I}_c from a parabolic fit of τ versus intensity in a small region of

TABLE I. The measured value of compensation intensity (\bar{I}_c) and the inferred size of C for various cells, polarization angles (α), and orientations (θ) of the cell's principal axis. The measured values of τ are shown when the laser is far detuned (τ_d) and when the cell's quadrupolar shift is compensated at $\nu = 0$, (τ_{\max}). Inferred values of the twist angle (θ) for a variety of cell shapes and sizes have been calculated. Cells *a* and *b* are cuboid cells while cells *c*, *p*, and *o* are all cylinders. All cells were coated with an alkene coating except for cell *o* which was coated with a polyethylene wax. All parameters are as defined in the text. A 2° uncertainty for all angles has been assumed throughout. A common global calibration uncertainty of 4% from the power meter has not been included. Inclusion of the nonlinear Zeeman effect would reduce all of the values of C by an inconsequential 0.08 mHz.

Cell	d/w (cm)	h (cm)	α	θ	τ_d (s)	τ_{\max} (s)	$I_c(\mu\text{W}/\text{cm}^2)$	C (mHz)	\mathcal{A}	l (cm)	$\langle\theta\rangle$ (mrad)
<i>a</i>	2.20 (5)	1.00 (2)	0°	0°	0.120	0.145	0.81 (3)	32 (1)	0.29	1.05	1.4 (1)
<i>a</i>	2.20 (5)	1.00 (2)	0°	20°	0.120	0.145	0.98 (3)	32 (2)	0.29	1.05	1.4 (1)
<i>a</i>	2.20 (5)	1.00 (2)	0°	45°	0.120	0.139	2.49 (8)	25 (5)	0.29	1.05	1.1 (2)
<i>a</i>	2.20 (5)	1.00 (2)	90°	90°	0.130	0.139	0.78 (3)	31 (1)	0.29	1.05	1.4 (1)
<i>b</i>	2.20 (5)	1.00 (2)	0°	45°	0.086	0.098	3.23 (10)	32 (7)	0.29	1.05	1.4 (3)
<i>c</i>	1.00 (5)	2.50 (5)	0°	90°	0.031	0.035	1.88 (13)	-38 (3)	-0.25	0.83	1.5 (2)
<i>p</i>	1.90 (1)	0.50 (1)	0°	0°	0.061	0.132	3.17 (16)	127 (6)	0.48	0.66	2.1 (3)
<i>o</i>	4.70 (10)	0.90 (6)	0°	0°	0.044	0.072	1.96 (14)	78 (6)	0.58	1.30	2.1 (3)

intensity near \bar{I}_c . The results and the inferred values of C are shown in Table I. It is reassuring that the value of C obtained by this method is consistent with that obtained from the full fit described in Appendix A. The agreement of the inferred values of C for the different polarization angles and cell orientations of cell a further supports our contention that we are indeed compensating the cell's quadrupolar shift with the tensor light shift. Of particular note is that when we rotate the cell's symmetry axis by 90° ($\alpha = 90^\circ$) the sign of $\Delta\nu_C$ reverses, allowing compensation at $\nu = 0$ only for $\theta > \theta_M$. It is also noteworthy that the far-detuned value of the effective spin-relaxation time, τ_d , rises when the cell is rotated, reflecting the anticipated factor of 2 reduction in the magnitude of $\Delta\nu_C$ [Eq. (3)].

To further investigate the role of cell shape in determining the quadratic shift we have measured the compensation intensity in a variety of other cells (Table I). Cell b is identical in shape to cell a and was coated with the same alkene coating. Though it exhibits an inferior spin-relaxation time, its measured value of C is compatible with that of cell a . Cell c is relatively long compared to its diameter. Here we expect and observe a reversal of the sign of C . The ‘‘pancake cell’’ (cell p) is a cylinder with a 1.9-cm diameter and a height of only 0.5 cm. As expected, this cell produces the largest value of C and impressively, its effective relaxation time more than doubles upon compensating its quadratic dephasing. All of these cells were coated with an alkene coating. Cell o was coated in 1999 with a polyethylene wax. We also attempted to measure a 2.2-cm-diameter sphere. Since we were unable to detect any enhancement of τ in this cell, it is not included in Table I. We note that the lack of enhancement in the sphere was anticipated since the cell has no quadrupolar anisotropy and hence should have no CIQS.

VI. EXTRACTING THE TWIST ANGLE AND A COMPARISON BETWEEN DIFFERENT CELLS

We use the model of Wu *et al.* to compare our measured shifts in different cells and to compare our results with those measured in other atomic systems [33]. In their model, the strength of the surface interaction is expressed in terms of the mean twist angle θ , the average rotation of the nuclear spin about the surface normal with each wall adhesion. The magnitude of the frequency shift of the polarization $|m\rangle\langle n|$ is given by their Eq. (117) as $v\mathcal{A}\langle\theta\rangle(m^2 - n^2)[3\cos^2(\alpha) - 1]/[4\pi l(2I - 1)]$, where \mathcal{A} is the cell's asymmetry parameter, $v = \sqrt{8kT/\pi M}$ is the mean thermal velocity of the atoms with mass M at temperature T , and the cell's characteristic length is defined to be $l = 4V/S$ where V and S are the volume and surface area of the cell. If we replace l with F in this equation and compare with our Eq. (3), we can express the mean twist angle of the *total* spin F , per wall adhesion, as

$$\langle\theta\rangle = 12\pi Cl(2F - 1)/v\mathcal{A}. \quad (4)$$

For a cylindrical cell, $l = (\frac{1}{2h} + \frac{1}{d})^{-1}$ and the asymmetry parameter is $\mathcal{A} = (d - h)/(d + 2h)$. We calculate that for symmetric cuboids the expressions for l and \mathcal{A} are identical with just the substitution of w for d . Using these expressions we infer the twist angles shown in Table I. For the alkene coated

cells a , b , and c there is good agreement with a weighted mean value of $\theta_{\text{Cs-alkene}} \approx 1.4$ mrad. We derive values of the twist angle for cells p and o that are about 2.1 mrad. Since cell o has a different coating, its departure from the mean is not surprising. However, the larger value observed in cell p is puzzling. The cell's small height has made the calibration of the average light intensity within the cell more difficult than in our other cells. There are also different varieties of alkene coating that may have been used on the different cells and other variations in the coating procedure and the cell's history that may be important [24]. Given these considerations, we will use the weighted average twist angle from the other three alkene coated cells in the remainder of this discussion. Clearly, future experiments in alkali cells with large quadrupolar anisotropies but different coatings would be useful.

VII. A COMPARISON WITH DIAMAGNETIC ATOMS AND THE PHYSICAL ORIGIN OF THE OBSERVED CIQS

It is instructive to compare our observed twist angles with those that have been observed in the diamagnetic atoms. Values of $\theta_{\text{Xe-pyrex}} = 38(4) \mu\text{rad}$ [10], and $\theta_{\text{Xe-silicon}} = 29 \mu\text{rad}$ [16] have previously been reported. Using Eq. (4) and the observed 50-mHz quadrupolar splitting in ^{201}Hg in a cuboid cell with dimensions in centimeters of $2 \times 2 \times 1$ we infer a value of $\theta_{\text{Hg-fused silica}} = 47 \mu\text{rad}$ [12]. Most of our comparisons will be made with $\theta_{\text{Xe-pyrex}}$ since it was the most extensively studied. We note that $\theta_{\text{Cs-alkene}}$ is about 37 times larger than $\theta_{\text{Xe-pyrex}}$.

In the following subsections we discuss three physical effects that can create CIQS in atoms. First, we discuss the CIQS created by a *nuclear* electric quadrupole moment (EQM) in an electric-field gradient. Then we consider the shift associated with an *atomic* EQM in an electric-field gradient. Finally, we examine the shift created by the static polarizability of the Cs ground state in the presence of surface electric fields.

A. Nuclear electric quadrupole moment

The observed CIQS of the diamagnetic atoms are usually explained as a shift created when the nuclear EQM experiences an electric-field gradient during the wall collision [10]. In general, the electric-field gradient at the nucleus is larger than that experienced by the atom by a factor traditionally known as the Sternheimer shielding or antishielding factor. The resulting quadrupolar shift is proportional to the product of the nuclear EQM, the Sternheimer factor, and the gradient of the electric field experienced by the atom. The nuclear EQMs of ^{201}Hg , ^{131}Xe , and ^{133}Cs in units of barns are, respectively, about 0.4, -0.114 and -0.004 [34] and their shielding factors are, respectively, about -47 [35], -154 [36], and -177 [37]. Combining these factors we expect that for comparable electric-field gradients on the atoms and comparable adsorption times on the walls that the magnitude of $\theta_{\text{Hg-fused silica}}/\theta_{\text{Xe-pyrex}}$ would be of order 1, as is observed. However, if this mechanism were responsible for our shift in ^{133}Cs we would expect $\theta_{\text{Cs-alkene}}/\theta_{\text{Xe-pyrex}}$ to be about 0.04. Since our observed twist angles are actually 37 times larger than those observed in ^{131}Xe , it is clear that this mechanism is inadequate to describe our current observations and that other mechanisms must be considered.

B. Atomic electric quadrupole moment

One alternative explanation is that we are observing a shift created by the interaction of the *atomic* EQM of the $F = 4$ hyperfine level of the Cs ground state with the electric-field gradients at the walls. The Cs ground state hyperfine levels acquire this static quadrupole moment through the admixing of d states into the nominal s state by the hyperfine interaction. Derevianko calculates the EQM of the hyperfine-perturbed $F = 4$ state to be $-1.6 \times 10^{-5} |e| a_0^2 = -418$ barns [38]. For comparable surface field gradients and adsorption times, we expect this EQM to yield a ratio of twist angles with magnitude $\theta_{\text{Cs-alkene}}/\theta_{\text{Xe-pyrex}} \approx 418/(154 \times 0.114) \approx 24$. Since we observe a twist angle per adsorption that is about 37 times larger than that observed in Xe, this model yields the correct sign and order of magnitude for the effect. To account for the full size of the observed effect would require the product of the electric-field gradient and the adsorption time to be about 50% larger for Cs on a 23 °C alkene surface than for Xe on a 70 °C pyrex surface. It appears likely that this mechanism makes a significant contribution to the observed effect.

C. Tensor polarizability of the Cs ground state

Another mechanism that could potentially contribute to our observations is due to the asymmetric electric fields (as opposed to the electric-field gradients previously discussed) experienced by the atoms during wall collisions. This asymmetric field produces a quadratic splitting due to the tensor polarizability of the Cs ground state. Because the Cs ground state has a total electronic spin of $\frac{1}{2}$, in the absence of the nuclear spin, no electronic tensor shift is possible. However, in third-order perturbation theory a static tensor polarizability of the ground state is produced through the hyperfine interaction. For the $F = 4$ level the shift has been calculated and measured and is described by the expression $\Delta\nu_T = -\frac{1}{2}\alpha_2 \frac{3m_l^2 - F(F+1)}{2I(2I+1)} [3\cos^2(\varphi) - 1] E^2$, where $\alpha_2 = -0.037(3)$ Hz/(kV/cm)² and φ is the angle between \mathbf{E} and \mathbf{B} [39]. If we reasonably assume that the average electric field during a wall collision is perpendicular to the surface then, when averaged over the cell, $\varphi = \alpha$. The effective average tensor shift induced in the atoms will be proportional to $A f E_s^2$ where E_s^2 is the average square of the electric field perpendicular to the surface, and $f = t_w v / l$ is the fraction of the time that an atom experiences this field; t_w is the average adsorption time per collision. If this mechanism is to describe our observed effect, it requires that $\Delta\nu_C = \Delta\nu_T$, implying that $E_s^2 = -4I(2I+1)C/A f \alpha_2$. Since α_2 is negative and we measure C/A to be positive in our cells, the tensor shift has the correct sign to account for our observed shift. To create the total observed shift would require an average value of $t_w E_s^2 \sim (4 \text{ MV/cm})^2 \text{ ns}$. For $t_w \sim 1 \text{ ns}$ [24] this would correspond to $E_s^2 \approx (0.04 \text{ V/\AA})^2$, a large but not unreasonable surface field.

To see if the requisite value of E_s^2 is compatible with other experimental observations, we examine the study of Corsini *et al.* of the hyperfine frequency shift in coated Rb cells [24]. The hyperfine frequencies they observe in their alkene-coated cells are typically shifted from their vacuum values by about -100 Hz in a 1-in.-diameter spherical ⁸⁵Rb cell

at 25 °C. It is well known that the clock transition they used is shifted in the presence of an electric field by $\Delta\nu_0 = k E^2$ where the constant $k = -1.24 \text{ Hz}/(\text{kV/cm})^2$ [40]. The atoms in their cell only experience this field for a fraction of the time $f = t_w v / l \sim 1.6 \times 10^{-5}$ for $t_w = 1 \text{ ns}$. As a consequence, if the observed shift were created by the surface electric field the value of the mean electric field squared would be given by the expression $f k E_s^2 \sim -100 \text{ Hz}$. This implies that $E_s^2 \sim (0.02 \text{ V/\AA})^2$. If the electric fields at the surface of the Cs and Rb cells are comparable, this would suggest that about a quarter of the observed quadrupolar shift we see might be due to the tensor polarizability. If so, presumably the remainder might be associated with the atomic quadrupole shift.

Clearly, additional modeling of the atom-wall interaction and further experiments will be required to determine with confidence the relative importance of the possible mechanisms we have explored here. An experiment that would measure both the hyperfine shift and the CIQS in the same cell could be particularly revealing.

VIII. CONCLUSIONS AND DISCUSSION

We have demonstrated that it is possible to measure and cancel the CIQS in a cell containing paramagnetic atoms. In cesium, measurement of the intensity and polarization angle that produce the greatest enhancement of τ at $\nu = 0$ is sufficient to determine the strength of the CIQS. The method developed here provides a tool for the investigation of the surface interactions of paramagnetic atoms. The coupling between the nuclear EQM and the cell's electric-field gradients that successfully describes CIQS in diamagnetic systems is not large enough to explain the effect we observe in cesium. We have discussed two alternative possibilities that could give substantial contributions to the CIQS in Cs. One involves the interaction of the atomic EQM with the cell's surface electric-field gradient while the second is due to the interaction between the Cs ground state tensor polarizability and the surface electric field. It appears that measurement of CIQS can provide a valuable probe of the surface electric field and/or its gradient. Similar investigations involving other atoms and other surfaces should help to unambiguously determine the fundamentals of the atom-surface interaction. Measurements of both the hyperfine shift and the CIQS in the same cell would certainly be useful and might have important implications for secondary frequency standards using atomic vapor cells.

The ability to cancel the CIQS could lead to improved precision in magnetometers that employ cells with large quadrupolar anisotropies. As we have demonstrated, τ can be increased by a significant factor. In addition, for the same laser intensity, the magnitude of the probe beam rotation at $\nu = 0$ is about five times greater than at the canonical detuning of 3 GHz. Together these factors could lead to improved magnetometer sensitivity. For precision measurements, where it is sometimes necessary to use nonspherical cells, there are other potential benefits to canceling the CIQS. Clearly, if an experiment is sensitive to a systematic effect that is proportional to the total quadratic splitting of the states, cancellation of the splitting would be desirable. However, one has to weigh carefully this benefit against the possibility of

increased sensitivity to systematic effects that might couple to the compensating tensor light shift. In such situations it may be more desirable to suppress the light shifts by operating with a polarization angle of θ_M .

While the approach outlined here is nearly ideally suited to Cs, we believe that it should be possible to apply it with some modification to other atoms. Rb seems like an excellent possibility, though additional care will have to be taken due to the smaller upper-state hyperfine splitting and the larger Doppler width. It may also be possible to apply the technique to ^{201}Hg now that narrow-band laser sources to excite the $6^1S_0-6^3P_1$ transition at 254 nm are available.

ACKNOWLEDGMENTS

We thank Dmitry Budker, Derek Kimball, Marianne Bouchiat, William Happer, Paul Vetter, and Eugene Commins for their insights and encouragement. We thank David DeMille and Steve Lamoreaux for an inspiring and clarifying discussion of the physical mechanisms likely to produce the observed quadrupolar frequency shift. We thank Brian Patton for his help with our polarimeters, Mike Souza for cell fabrication, Mikhail Balabas for cell coating, and Dmitry Budker for the loan of several vapor cells. We thank Andrei Derevianko for calculating the Cs $6S$ quadrupole moment. D.G.A. would like to acknowledge the Schupf Fellowship and N.L. would like to thank the Amherst College Summer Science Research program for support. This work was supported by NSF Grant No. PHY1205824 and No. PHY1519265.

APPENDIX: MODELING THE OBSERVED FREQUENCY AND INTENSITY DEPENDENCE OF τ

In order to model the intensity and frequency dependence of τ we need to quantify the three important decay rates: (1) a scalar rate R_{\min} that is independent of frequency and intensity, (2) a depolarization rate R_a that is proportional to the rate of absorption on the atomic resonance lines, and (3) an effective decay rate R_Q that depends on the size of the total quadratic splitting induced in the atoms by the sum of the light shift and a frequency-independent CIQS.

The scalar rate, R_{\min} , is primarily due to depolarization of the atom during scattering with the wall or cell stem. It is independent of the frequency and intensity of the probe beam. In the absence of all other decay mechanisms, it determines the maximum value of the spin-relaxation time, τ_{\max} , through the relationship $R_{\min} = 1/\tau_{\max}$. A single value of τ_{\max} is assumed for all of the fit data.

The absorption depolarization rate is modeled as $R_a = [d_3 V_3(\nu) + d_4 V_4(\nu)]\bar{I}(\nu)$ where $V_3(\nu)$ and $V_4(\nu)$ are the Voigt profiles shown in Fig. 3, $\bar{I}(\nu)$ is the light intensity at frequency ν , and d_3 and d_4 are fit parameters. Since these absorptive decay rates are dependent on optical pumping and the degree of saturation, we allow d_3 and d_4 to assume different values for scans taken at different laser intensities.

To relate the effective polarization decay rate, R_Q , associated with the quadrupole dephasing to the magnitude of the total quadrupolar shift we simulate the time evolution of the initially polarized $F = 4$ state in the presence of both the Zeeman and quadrupolar Hamiltonians. Specifically, we use

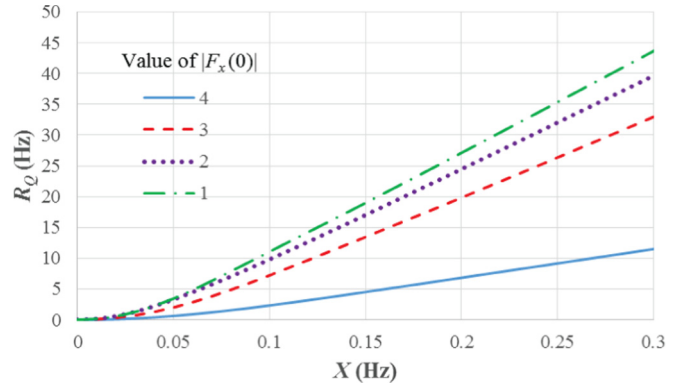


FIG. 4. The calculated effective quadrupolar decay rate R_Q as a function of the net strength of the quadrupolar splitting X . The solid (blue) line, dashed (red) line, dotted (violet) line and dash-dot (green) lines correspond respectively to $|F_x(0)| = 4, 3, 2$ and 1 .

MATHEMATICA to calculate the time evolution of the different eigenstates of the F_x operator for $F = 4$. The expectation value of F_x should be proportional to the optical rotation we observe in our experiment. We allow each of the F_x eigenstates to evolve in the presence of a Hamiltonian that is the sum of the Zeeman and the CIQS Hamiltonians $H = h\Delta\nu_{\text{Zeeman}} + hX[3m_F^2 - F(F+1)]$ where h is Planck's constant and $X = C[3\cos^2(\alpha) - 1] + A(\nu)[3\cos^2(\theta) - 1]\bar{I}$. To simulate our experimental signals, we calculate the expectation value of F_x as a function of time and multiply it by $e^{-t/\tau_{\max}}$ to account for the scalar decay rate R_{\min} . As in the real experiment, the simulated decaying oscillation is fit to Eq. (1) over a 0.3-s interval and an effective decay rate $R = 1/\tau$ is extracted. For small values of the quadratic shift we retrieve the expected relaxation time τ_{\max} . As the value of the quadratic shift is increased the effective lifetime decreases due to the dephasing of the eight different frequencies between adjacent magnetic sublevels. For each value of X we extract an “effective” quadrupolar decay rate, $R_Q = R - R_{\min}$. A plot of R_Q as a function of X for each of the F_x eigenstates is shown in Fig. 4. For small values of X the decay rate R_Q rises quadratically as one would expect from a beat envelope proportional to the cosine of the difference frequency. For larger values of X , R_Q becomes approximately linear in X . The calculated rates are smaller for larger magnitudes of the initial polarization, $|F_x(0)|$. This result can be traced to the fact that the F_x eigenstates with large $|F_x(0)|$ have smaller amplitudes of high $|m_F|$ states. Since the quadratic splittings between adjacent magnetic sublevels are largest for large $|m_F|$, the states with high values of $|F_x(0)|$ decohere less rapidly.

We do not know the initial value of $F_x(0)$ after pumping. We began by assuming that all of the atoms were in the stretched state with $F_x(0) = 4$. We found that this assumption did not produce a large enough value of R_Q to match our data. To achieve a better fit to the data we instead assumed that we have a mix of $F_x(0) = 4$ and $F_x(0) = 3$ with relative fractions given, respectively, by β and $(1-\beta)$. The parameter β is a global fit parameter in our model.

Our model values of τ are determined using the expression $\tau = 1/(R_{\min} + R_a + R_Q)$. Since we only expect this model to be applicable in regions of modest absorption, we do not

attempt to fit data within 315 MHz of the 4-3 and 4-4 line centers. We have done a single least-squares minimization using all of the data shown in Figs. 2(a) and 2(b) to determine the optimal fit parameters. We find that the data shown are consistent with values of $\tau_{\max} = 0.143$ s, $\beta = 0.73$, and $C = 0.029$ Hz. The resulting fits to the data at $\theta = 0^\circ$ and $\theta = 70^\circ$ are shown as the solid lines in Figs. 2(a) and 2(b).

Despite the simplicity and limitations of the model, it does capture the key features of our data surprisingly well. Several aspects of the fits merit discussion. First, and most important, the measured decay rates are compatible with those predicted from the model using a reasonable admixture of the $F_x(0) = 3$ and $F_x(0) = 4$ states. Though the model does slightly overpredict τ for the central region of the lowest-intensity

scan with $\theta = 0$, it does correctly predict its flattening near the line center. This flattening is a result of the negative maxima in the light shift predicted near $|\nu| \approx 300$ MHz (Fig. 3). The compensation intensity at these frequencies is predicted to be lower than the compensation intensity at $\nu = 0$. By itself, this would result in larger values of τ at these frequencies at low intensity. However, unlike $\nu = 0$, these points experience significant absorption that reduces τ . The competition between these opposing tendencies renders τ approximately flat over this central frequency range. We note that in Rb, due to its smaller upper-state hyperfine structure and broader Doppler width, this central decrease in the magnitude of $A(\nu)$ is not expected [19]. As a consequence, no similar flattening in this region would be anticipated in Rb.

-
- [1] D. Budker and D. F. J. Kimball, *Optical Magnetometry* (Cambridge University Press, New York, 2013).
- [2] W. Happer, Y.-Y. Jau, and T. G. Walker, *Optically Pumped Atoms* (Wiley-VCH, Germany, 2010).
- [3] D. Budker and M. Romalis, *Nat Phys* **3**, 227 (2007).
- [4] J. H. Simpson, *Bull. Am. Phys. Soc.* **23**, 394 (1978).
- [5] C. H. Volk, J. G. Mark, and B. C. Grover, *Phys. Rev. A* **20**, 2381 (1979).
- [6] T. M. Kwon, J. G. Mark, and C. H. Volk, *Phys. Rev. A* **24**, 1894 (1981).
- [7] P. A. Heimann, I. A. Greenwood, and J. H. Simpson, *Phys. Rev. A* **23**, 1209 (1981).
- [8] P. A. Heimann, *Phys. Rev. A* **23**, 1204 (1981).
- [9] Z. Wu, W. Happer, and J. M. Daniels, *Phys. Rev. Lett.* **59**, 1480 (1987).
- [10] Z. Wu, W. Happer, M. Kitano, and J. Daniels, *Phys. Rev. A* **42**, 2774 (1990).
- [11] S. K. Lamoreaux, J. P. Jacobs, B. R. Heckel, F. J. Raab, and E. N. Fortson, *Phys. Rev. A* **39**, 1082 (1989).
- [12] P. K. Majumder, B. J. Venema, S. K. Lamoreaux, B. R. Heckel, and E. N. Fortson, *Phys. Rev. Lett.* **65**, 2931 (1990).
- [13] T. E. Chupp and R. J. Hoare, *Phys. Rev. Lett.* **64**, 2261 (1990).
- [14] S. Appelt, G. Wackerle, and M. Mehring, *Phys. Rev. Lett.* **72**, 3921 (1994).
- [15] R. Butscher, G. Wackerle, and M. Mehring, *J. Chem. Phys.* **100**, 6923 (1994).
- [16] E. A. Donley, J. L. Long, T. C. Liebisch, E. R. Hodby, T. A. Fisher, and J. Kitching, *Phys. Rev. A* **79**, 013420 (2009).
- [17] M. V. Balabas, T. Karaulanov, M. P. Ledbetter, and D. Budker, *Phys. Rev. Lett.* **105**, 070801 (2010).
- [18] W. Happer and B. S. Mathur, *Phys. Rev.* **163**, 12 (1967).
- [19] B. S. Mathur, H. Tang, and W. Happer, *Phys. Rev.* **171**, 11 (1968).
- [20] K. F. Zhao, M. Schaden, and Z. Wu, *Phys. Rev. Lett.* **103**, 073201 (2009).
- [21] S. K. Lamoreaux, J. P. Jacobs, B. R. Heckel, F. J. Raab, and E. N. Fortson, *Phys. Rev. Lett.* **57**, 3125 (1986).
- [22] K. Jensen, V. M. Acosta, J. M. Higbie, M. P. Ledbetter, S. M. Rochester, and D. Budker, *Phys. Rev. A* **79**, 023406 (2009).
- [23] W. Chalupczak, A. Wojciechowski, S. Pustelny, and W. Gawlik, *Phys. Rev. A* **82**, 023417 (2010).
- [24] E. P. Corsini, T. Karaulanov, M. Balabas, and D. Budker, *Phys. Rev. A* **87**, 022901 (2013).
- [25] L. R. Hunter, J. E. Gordon, S. K. Peck, D. Ang, and J.-F. Lin, *Science* **339**, 928 (2013).
- [26] S. K. Peck, D. K. Kim, D. Stein, D. Orbaker, A. Foss, M. T. Hummon, and L. R. Hunter, *Phys. Rev. A* **86**, 012109 (2012).
- [27] S. A. Murthy, D. Krause, Jr., Z. L. Li, and L. R. Hunter, *Phys. Rev. Lett.* **63**, 965 (1989).
- [28] W. C. Griffith, M. D. Swallows, T. H. Loftus, M. V. Romalis, B. R. Heckel, and E. N. Fortson, *Phys. Rev. Lett.* **102**, 101601 (2009).
- [29] D. F. J. Kimball, I. Lacey, J. Valdez, J. Swiatlowski, C. Rios, R. Peregrina-Ramirez, C. Montcrieffe, J. Kremer, J. Dudley, and C. Sanchez, *Ann. Phys.* **525**, 514 (2013).
- [30] E. Zhivun, A. Wickenbrock, J. Sudyka, S. Pustelny, B. Patton, and D. Budker, [arXiv:1511.05345v1](https://arxiv.org/abs/1511.05345v1).
- [31] J. M. Amini and H. Gould, *Phys. Rev. Lett.* **91**, 153001 (2003).
- [32] D. Dipankar and N. Vasant, *J. Phys. B: At., Mol. Opt. Phys.* **39**, 2013 (2006).
- [33] Z. Wu, S. Schaefer, G. D. Cates, and W. Happer, *Phys. Rev. A* **37**, 1161 (1988).
- [34] N. J. Stone, *At. Data Nucl. Data Tables* **90**, 75 (2005).
- [35] J. A. Shea and E. J. Campbell, *J. Chem. Phys.* **81**, 5326 (1984).
- [36] E. J. Campbell, L. W. Buxton, M. R. Keenan, and W. H. Flygare, *Phys. Rev. A* **24**, 812 (1981).
- [37] F. D. Feiock and W. R. Johnson, *Phys. Rev.* **187**, 39 (1969).
- [38] A. Derevianko, *Phys. Rev. A* **93**, 012503 (2016).
- [39] S. Ulzega, A. Hofer, P. Moroshkin, and A. Weis, *Europhys. Lett.* **76**, 1074 (2006).
- [40] E. J. Angstmann, V. A. Dzuba, and V. V. Flambaum, *Phys. Rev. Lett.* **97**, 040802 (2006).